Available online at www.sciencedirect.com

ScienceDirect

Proceedings of the Combustion Institute 38 (2021) 6713–6722

Proceedings of the Combustion Institute

www.elsevier.com/locate/proci

Experimental feasibility of tailored porous media burners enabled via additive manufacturing

Sadaf Sobhani [a,b,*], Priyanka Muhunthan [b], Emeric Boigné [b], Danyal Mohaddes [b], Matthias Ihme [b]

[a] *Sibley School of Mechanical and Aerospace Engineering, Cornell University, Ithaca, NY 14853, USA*
[b] *Department of Mechanical Engineering, Stanford University, Stanford, CA 94305, USA*

Received 7 November 2019; accepted 28 June 2020
Available online 27 August 2020

Abstract

The advantages in performance and emissions from combustion within the voids of a porous material, as compared to those of conventional open-flame combustion, have motivated numerous studies to understand and harness the connection between the underlying porous structure topology and the desired system-level properties. The current study examines the feasibility and performance of additively manufactured complex ceramic structures with geometric functionalization to actualize novel porous media burner design concepts for enhanced performance. Smoothly graded porous structures are synthesized using triply periodic minimal surfaces and manufactured via lithography-based ceramic manufacturing. Experiments are performed on these structures to characterize flame stability, axial temperature profiles, and pressure drop for three different pore-scale topologies. These measurements are complimented by computational predictions from one-dimensional volume-averaged models. X-ray computed tomography was used to verify relevant geometric properties of the structures, as well as to examine the material after combustion. This work demonstrates the first smoothly graded burner, leveraging recent advancements in additive manufacturing to design, fabricate, and test the performance of burner concepts unattainable by traditional ceramic foam manufacturing techniques.

Keywords: Porous media burners; Ceramic additive manufacturing; Triply periodic minimal surfaces

1. Introduction

Experimental and numerical studies have shown that Porous Media Burners (PMBs) can exhibit significant advantages over conventional free-flame systems [1–4]. Through excess enthalpy combustion, PMBs recirculate heat from combustion products to incoming reactants, leading to increased power output, faster flame speeds, extended flammability limits, and reduced emissions [5]. Applications for PMBs include gas turbines, reformers, and fuel cell afterburners [6].

Flame stabilization in PMBs is a complex phenomenon that depends on a combination of

* Corresponding author at: Sibley School of Mechanical and Aerospace Engineering, Cornell University, Ithaca, NY 14853, USA.
E-mail address: sobhani@cornell.edu (S. Sobhani).

https://doi.org/10.1016/j.proci.2020.06.120
1540-7489

thermal and fluid transport processes. A common PMB design is the interface-stabilized step burner, which enables flame stabilization at the interface between low and high pore-density porous materials [7]. To prevent flash-back, a low thermally conductive material is commonly used in the low pore-density section, thereby limiting effective heat recirculation to the incoming reactants. Recently, a new burner design was proposed that relies on a graded burner topology to enhance flame stabilization and heat recirculation [8]. Since smooth pore-scale gradations in ceramic structures are not accessible through traditional manufacturing techniques, the previous study showed that stepwise graded burner topologies lead to enhanced heat exchange and significant extension of stability limits in comparison to interface-stabilized burner designs [8].

Due to the high-temperature and corrosion resistance requirements, high-performance ceramics are most commonly used in PMBs, including Silicon Carbide (SiC), Alumina (Al_2O_3), and Yttria-Stabilized Zirconia (YZA). Several manufacturing processes have been developed to produce porous ceramic foams, including replication, direct foaming, and chemical vapor deposition techniques [9,10]. Previous efforts to design PMBs have been limited to those that can be rendered by these traditional ceramic foam manufacturing techniques, which are characterized only by bulk properties (e.g. pore-density, averaged pore-size, etc.) rather than local pore-size or porosity. Additionally, traditional techniques result in random strut orientations and varying pore-distributions, which can significantly alter local flow and flame properties. Control of the burner geometry and material properties would enable experimental repeatability and tailoring for specific system requirements such as pressure drop, flame-stabilization, or heat output. Recent advances in Additive Manufacturing (AM) introduce opportunities to modulate the porous media topology and composition, yet so far, the use of AM to PMB applications has not been explored.

The goal of this study is to examine the feasibility and performance of additively manufactured ceramic structures in PMBs. Building upon previous work [8], three graded topology burner designs are first studied using a one-dimensional volume-averaged model. Trends in flame stability, pressure drop, and emissions associated with the burner design are studied (Section 2). One-dimensional topology profiles are then translated to three-dimensional structures by applying the triply periodic minimal surface equations (Section 3.1) and subsequently manufactured using Lithography-based Ceramic Manufacturing (LCM) (Section 3.2). In LCM, as well as in many other AM techniques, the properties of the final product depend heavily on the conditions at different manufacturing stages, including suspension composition, chamber temperature, and direction of printing. As such, each sample in this study is analyzed using X-ray Computed Tomography (XCT) in order to extract important geometric characteristics of the printed burners and later to examine the post-combustion material. Next, the fabricated burners are experimentally tested to observe flame stability and identify trends in temperature profiles and pressure drop. The experimental setup is described in Section 4 and subsequent results are discussed in Section 5. Model predictions are shown to accurately capture trends found in the experimental results. Conclusions are presented in Section 6 along with comments on potential future work.

2. Computational analysis

Numerical simulations were performed using the Cantera [11] 1D reacting flow solver, which was adapted to account for the coupling between the gas and solid phases. More details on the model assumptions, boundary conditions, and the computational method can be found in [8]. Detailed reaction chemistry, including nitrogen, for methane/air was modeled using the GRI 2.11-mechanism [12]. Using this simulation methodology, a parametric study exploring inlet mass flux and equivalence ratio was carried out to compare the stability range of various graded burner designs with equivalent averaged geometric properties. Starting with a stable operating point, simulations were performed in which the mass flux rate is incrementally increased or decreased until the solver does not find a steady-state solution or the flame nears the ends of the computational domain.

Three different permutations of a graded PMB were investigated with the equivalent averaged pore-size ($\bar{d} = 1.47$ mm) and porosity ($\bar{\epsilon} = 0.8$) but varying gradations: Burner A has both linearly increasing pore-diameter ($d_1 = 0.39$, $d_2 = 2.54$ mm) and porosity ($\epsilon_1 = 0.75$, $\epsilon_2 = 0.85$); Burner B has constant porosity ($\epsilon = 0.8$) and linearly increasing pore-diameter ($d_1 = 0.39$, $d_2 = 2.54$ mm); and Burner C has constant pore-diameter ($d = 1.47$ mm) and linearly increasing porosity ($\epsilon_1 = 0.75$, $\epsilon_2 = 0.85$).

Results from this parametric study are presented in Fig. 1, where the stability regime is bounded by flame extinction conditions at the low-mass flux limit and blow-off at the high-mass flux limit. These simulations predict that all burner designs have low NO_x and CO emissions (i.e. < 10 ppm) and that pressure drop is below 6.5% for all operating conditions. As illustrated, Burner B, with constant porosity and increasing pore-diameter has the largest stability regime. At mutually equivalent stable operating conditions, Burner B has lower NO_x and CO emissions as compared to those for Burner A, where the porosity is also increasing. Burner C,

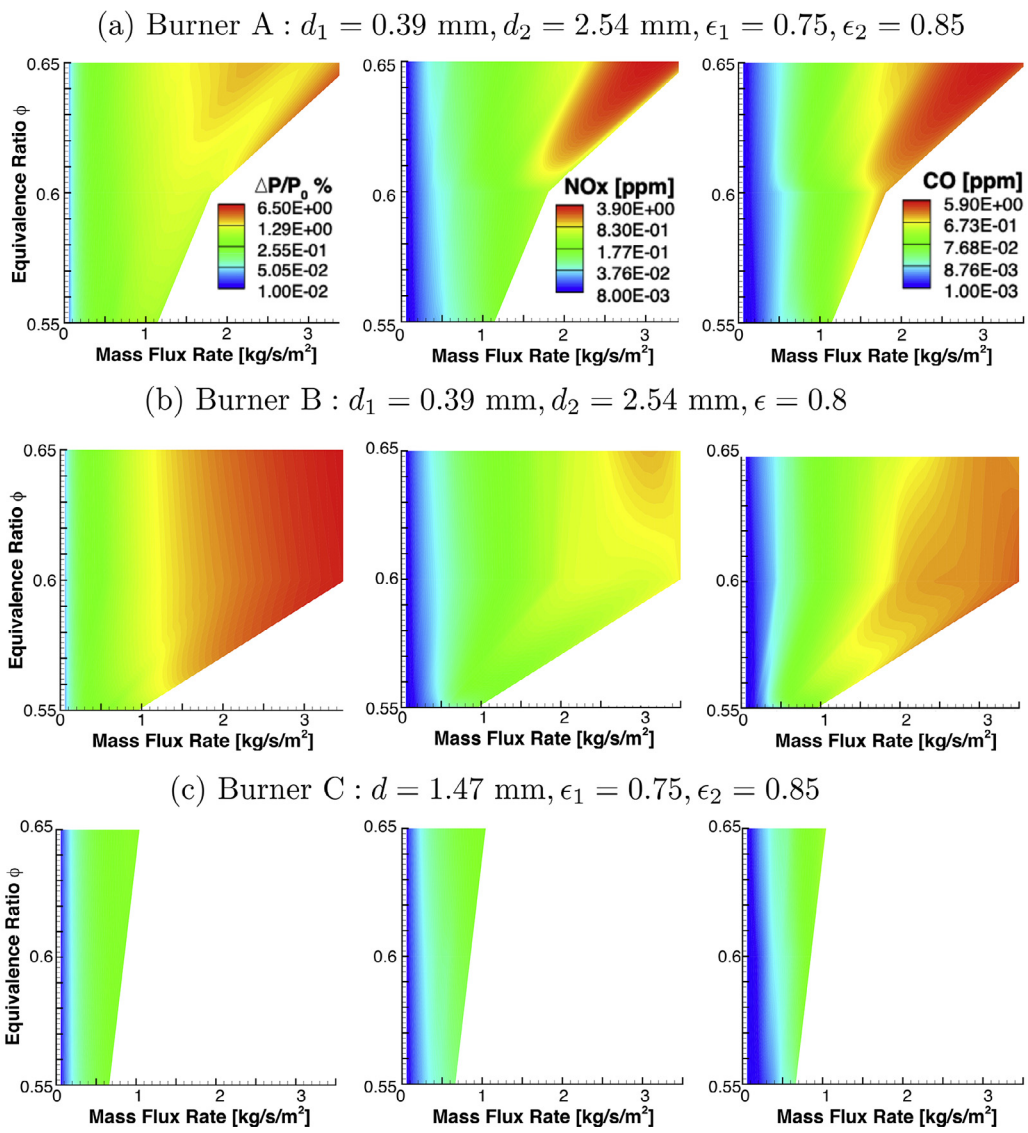

Fig. 1. Computational results for the three linearly graded burner geometries with equivalent averaged geometric properties, (left) pressure drop, (middle) NO_x, and (right) CO emissions.

which is graded only in porosity, has the smallest stability envelope and comparable pressure drop and emissions as the other burners at mutually stable operating conditions. Burner A has lower pressure drop as compared to Burner B, due to regions of higher porosity.

As illustrated, burners with equivalent averaged geometric properties are predicted to vary significantly in performance, due to variations in heat recirculation and interphase heat exchange [8]. The results imply a significant potential for optimizing the underlying porous structure according to the desired performance metrics (i.e. emissions, pressure drop, flame stability).

In the following section, designs corresponding to the computational graded Burners B and C were targeted in order to experimentally verify the large performance variation predicted by the model.

3. Burner design and manufacturing

3.1. Design of burner geometry

PMBs are commonly designed using stochastic foams that provide limited control over the pore topology. To overcome this limitation, Triply Periodic Minimal Surfaces (TPMS) are used in this

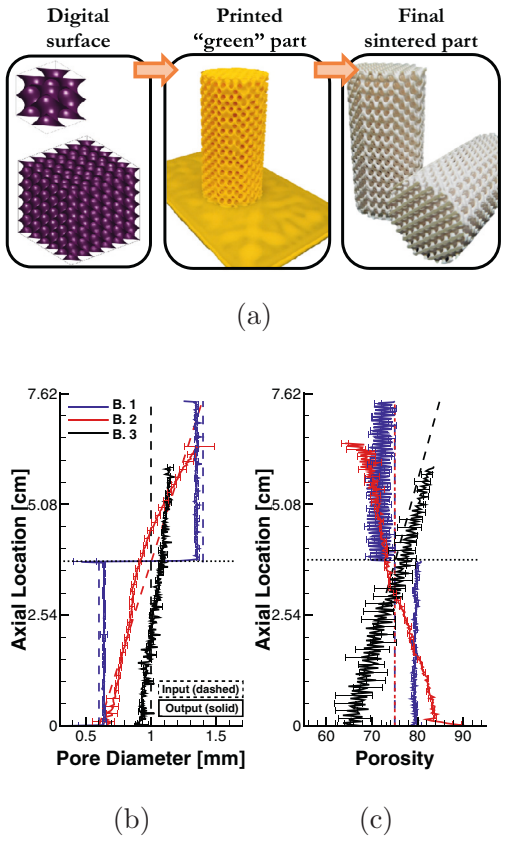

Fig. 2. (a) Additive manufacturing process with the digital surface unit cells, printed "green" (i.e. pre-thermal treatment) part, and final sintered part, (b) pore diameter and (c) porosity profiles of printer-input (dashed line, see Table 1) and printer-output (solid line) geometries. The dotted horizontal line indicates the interface of Burner 1.

work to design functionally graded porous structures with high surface-to-volume ratio and interconnectivity [13]. TPMS are represented by a geometric function $F(x, y, z)$ that is comprised of a combination of harmonic terms [14]. $F = 0$ represents the iso-surface that separates solid ($F \leq 0$) and void ($F > 0$) regions.

In the current study, D-type surfaces were used to create porous foam-like structures, which are parameterized by the following expression:

$$F = \sin\left[\sum_{i=1}^{3} px_i\right] + 2\prod_{i=1}^{3}\sin(px_i) + q, \tag{1}$$

where $x_i = [x, y, z]^\intercal$, and p and q are parameters controlling the pore-size and porosity, respectively. The structure of the D-type surface is illustrated in Fig. 2(a), together with images of the printed structure.

To achieve a graded design along the axial direction z, $p(z)$ and $q(z)$ were varied in the axial direction according to the following equations: $p(z) = p_1 + (p_2 - p_1)\, z/L$, $q(z) = q_1 + (q_2 - q_1)\, z/L$, where L is the length of the sample, and subscripts 1 and 2 refer to the calculated limits of p and q that are based on the desired limits of pore-size and porosity, respectively. The porosity $\epsilon(z)$ of the burners can be calculated as follows:

$$\epsilon(z) = \frac{1}{\delta V}\iiint_{\delta V}(F > 0)\, dx\, dy\, dz, \tag{2}$$

where $\delta V = A\delta Z$, A is the cross-sectional area and δZ is the axial section thickness used to compute an averaged quantity at a given axial location, z. The pore-diameter $d(z)$ is computed as follows:

$$d(z) = 2\left[\frac{3}{4\pi}\frac{\epsilon(z)\delta V}{N_{\text{pores}}(z)}\right]^{1/3}, \tag{3}$$

where $N_{\text{pores}}(z)$ is the total number of pores in δV.

Table 1
Geometric properties of the printer-input structures, each 20 mm in diameter and 75 mm in length.

Burner	Pore-diameter	Porosity
1	0.6–1.4 mm (Step)	75% (Constant)
2	0.6–1.4 mm (Linear)	75% (Constant)
3	1.0 mm (Constant)	65–85% (Linear)

Each of the three burners was 20 mm in diameter and 75 mm in length. The prescribed geometric properties of the burners are illustrated in Fig. 2(b) and (c) and outlined in Table 1 for additional clarity. Experimental Burner 1 was comprised of two consecutive homogenous porous structures with two different pore-diameters, while experimental Burner 2 was linearly graded in pore-diameter, to compare the performances of the step versus graded PMBs. Experimental Burner 3 was linearly graded in porosity, to test the dependence of flame behavior on porosity versus pore-diameter gradation. Eq. (3) is used to approximate a representative pore size from the prescribed surface equation while XCT-diagnostics described in Section 3.3 enables geometric analysis of the printer-output parts. To facilitate pore-diameter comparisons with the XCT analysis, a ratio of 2.5 was found to relate the pore diameter from applying Eq. 3, which assumes simplified spherical pores, to that approximated from image analysis.

3.2. Manufacturing of burners

In AM, parts are created with Computer-Aided Design (CAD) and printed in layers through a variety of methods. Current ceramic AM technologies mainly fall into two categories: direct methods, which enable rapid fabrication in a single step, and multi-step indirect methods, which are more suitable for printing complex shapes [15]. Lithography-based methods are a subset of indirect techniques

that rely on selective space-resolved exposure to light to solidify the liquid suspension. In the present study, Digital Light Processing (DLP) is used to perform Lithography-based Ceramic Manufacturing (LCM) to demonstrate the feasibility of fabricating functionally graded Al_2O_3 matrix structures. In LCM, a liquid suspension of ceramic particles is photopolymerized by light using a digital light projector. The resulting "green part" is cleaned, thermally treated to remove organic material, and then sintered to produce the final part, as shown in Fig. 2(a). Further information on the additive manufacturing process and material properties of the Al_2O_3 foams is provided in [16].

3.3. XCT analysis

XCT imaging was used to assess the fidelity of the printing technology in reproducing the input geometry. The samples were scanned using a ZEISS Xradia 520 Versa X-ray microscope with a spatial resolution of 12 μm. The reconstructed images were smoothed using a 2D bilateral filter and then binarized with a 3D constant threshold. The porosity was calculated along the axial direction of the sample as the ratio of gas voxels to the total number of voxels, averaged over each cross-sectional slice. The pore and cell-diameters were identified using a 3D distance transform watershed algorithm and a 3D particle analyzer [17,18].

Results for the mean pore-diameter and porosity for each cross-sectional slice along the burners are shown in Fig. 2(b) and (c), respectively. Although the printed burner geometries deviate from the original designs, the general trends are well captured in the manufactured foams, given uncertainties in the fabrication process. Burner 2 had an approximately linear pore-diameter profile in the axial direction, although its porosity slightly decreased along the length of the burner. The same slight deviations are found in Burner 1, therefore Burners 1 and 2 remain topologically similar. The porosity profile of Burner 3 was close to that of the input, however while its pore-diameter was relatively constant, the value deviated slightly from that originally specified.

4. Experimental setup and procedure

Following the characterization of the matrix topologies, an experiment was conducted to investigate the performance and stability of the different burners. The experimental setup and instrumentation was detailed in previous work [8].

Methane and air were supplied from compressed gas cylinders and their flow rates were metered with mass flow controllers (MFCs). The burners were placed above a bed of packed stainless steel beads that served as a flashback arrestor. Six K-type mineral-insulated thermocouples (Watlow) were placed between the burner and insulation to measure temperature and observe trends in flame location. The thermocouples were spaced 60° azimuthally to monitor the flame alignment and were placed at the heights shown in the symbols corresponding to the experimental results of Fig. 4. An Omega PX309 pressure transducer was placed directly upstream of the burner to measure gauge pressure. Errors reported by the manufacturer were $\pm 1\%$ of the measured value for the MFCs, $\pm 0.75\%$ of the measured value for the thermocouples, and $\pm 0.25\%$ of 1 psi for the pressure transducer.

To observe stability behavior, the mass flux rates and equivalence ratios were systematically changed to test burner performance over a range of operating conditions. Stable operation and blow-off were defined according to the descriptions in [8]. Incrementally decreasing mass flux eventually resulted in either flash-back or extinction. Flash-back was considered to have occurred when the temperature recorded by the thermocouple furthest upstream was greater than 1000 K. Extinction was observed at the mass flux below which the flame would extinguish. Once the stability limits for a certain equivalence ratio had been identified, the equivalence ratio was changed by $\Delta\phi = 0.05$, and the previous process was repeated to produce a complete stability map for each burner.

5. Results and discussion

5.1. Stability maps

The burners tested in this study exhibited varying temperature profiles and stability regimes as a result of their unique geometries. However, there were several trends common to all burners. In general, higher equivalence ratios led to higher blow-off and reduced extinction limits. The increased flame temperatures at higher equivalence ratios enhances preheating of the inlet mixture, leading to extended stability limits. Although PMBs typically extend the lean flammability limit by raising the temperature of the incoming reactants [5], this behavior was not observed in this study due to significant radial heat losses caused by the small burner size and subsequently high surface area-to-volume ratio.

As illustrated in the stability maps in Fig. 3, graded Burner 2 outperformed the equivalent step Burner 1 and did not exhibit flash-back at any of the tested conditions. Previous work predicts that smooth gradations enhance solid–gas heat transfer, as quantified by the Stanton number [8], thus leading to a wider range of stable operating conditions. Due to the large radial heat losses, the overall burner stability is decreased as compared to that reported in the previous study with larger burner

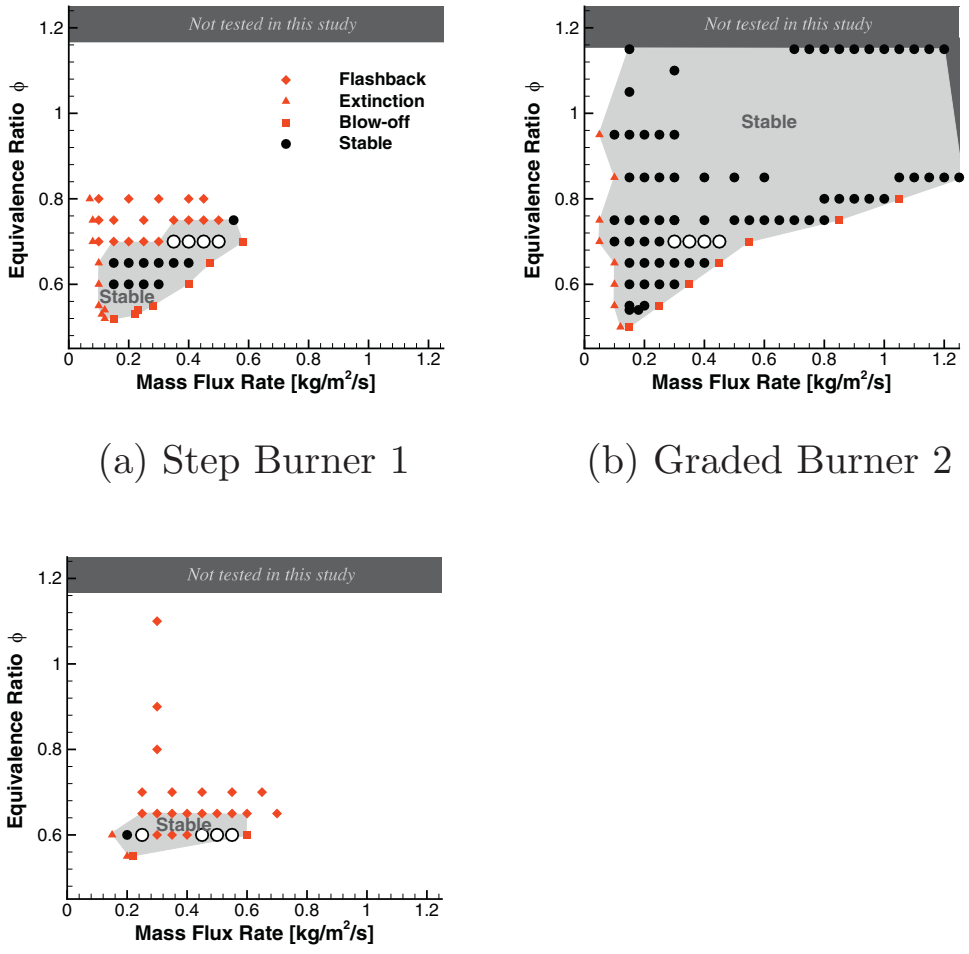

Fig. 3. Stability maps for for Burners 1–3. The open symbols correspond to conditions for which temperature profiles are discussed in Section 5.2.

diameters [8]. Although Burner 1 had a slightly larger stability regime than Burner 3, it exhibited flash-back with increasing equivalence ratio. Flash-back was commonly observed in Burner 3 due to the larger pore-sizes near the inlet allowing the flame to propagate upstream. The open symbols in Fig. 3 correspond to operating conditions for which temperature profiles are discussed in the following section. Due to the limitations of the constitutive models and assumptions invoked in the mathematical model, the computational model does not quantitatively predict the stability limits. However, the qualitative trends in flame stability from the experimental results compare well with the numerical analysis presented in Section 2. The geometric profile of the computational graded Burner B and C are comparable with that of the experimental Burners 2 and 3, respectively. As shown Figs. 1 and 3, the trend in flame stability is similar among the corresponding burners with regard to the total area of the stability regime. Thus, the simulation tool and fabrication methodology presented in this work can be applied to capture key trends in desired performance metrics and effectively actualize novel designs.

5.2. Temperature profiles

The temperature measurements for all burners are shown in Fig. 4. Fig. 4(b) illustrates the dynamic flame stabilization for Burner 2 with graded pore-diameter. In contrast, flames in Burner 1 are anchored at the interface for all stable operating conditions (Fig. 4(a)). Fig. 4(c) illustrates that most

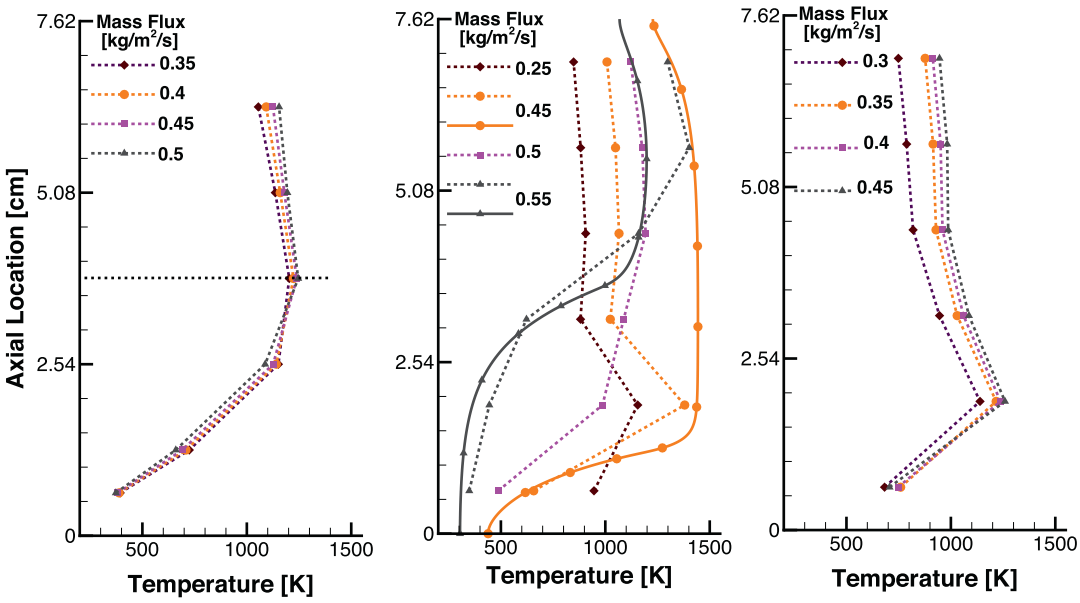

(a) B.1, ϕ = 0.7 (b) B.2, ϕ = 0.7 (c) B.3, ϕ = 0.6

Fig. 4. Experimental (dashed lines) and computational (solid lines) temperature profiles. The black horizontal dotted line indicates the interface of the two porous media in (a).

flames in Burner 3 were close to the flash-back limit and stabilized near the inlet as a result of the large pores in this section.

As shown in Fig. 4(b), the computational model outlined in Section 2 captures the dynamic flame stabilization, mostly exhibited in Burner 2. However, due to uncertainties in the closure models used in the simulations and those of the thermocouple measurements, the results differ quantitatively. In this comparison, the solid temperature from the simulations is compared to thermocouple measurements, since the thermocouple inserted inside a porous medium estimates the local solid temperature [19].

5.3. Pressure drop

The experimentally determined pressure drop for the burners was calculated and compared to theoretical values predicted using the Darcy–Forchheimer equation [20]:

$$\Delta P(z) = -\int_0^z \frac{\mu}{K_1 \rho}\frac{\dot{m}}{\epsilon A} + \frac{1}{K_2 \rho}\left(\frac{\dot{m}}{\epsilon A}\right)^2 dz \qquad (4)$$

where K_1 is the intrinsic permeability and K_2 is the non-Darcian drag coefficient, estimated using Ergun's equations [21]:

$$K_1 = \frac{d^2\epsilon^3}{150(1-\epsilon)^2}, \quad K_2 = \frac{d\epsilon^3}{1.75(1-\epsilon)}, \qquad (5)$$

The axial variation in thermoviscous properties across the flame was approximated as a step function and obtained from the simulation of a 1D, freely propagating flame in Cantera [11]. Pore-diameter and porosity were approximated from XCT analysis of the burners (Section 3.3).

Fig. 5 (a) illustrates the effect of the burner geometry on pressure drop. Although the topologies of Burners 2 and 3 were, on average, the same, the variation in local geometry led to a significant difference in predicted and experimental pressure drops. From Section 3.3, Burner 2 was characterized by small pores and high porosity at its inlet, and larger pores and lower porosity near its outlet. Eq. (4) shows that the pressure drop is more sensitive to porosity than pore-diameter ($\Delta P \propto \epsilon^{-5}, d^{-2}$). As a result, the decrease in pressure drop from the large pores at the outlet of Burner 2 was offset by the increase in pressure drop from the low porosity in the same section. In contrast, Burner 3 had a relatively constant pore-size, approximately equal to the average pore-diameter of Burner 2, and a linearly increasing porosity profile from inlet to outlet that led to lower theoretical and experimental pressure drops.

The effect of dynamic flame stabilization on pressure drop is shown in Fig. 5(b) for Burner 2 at $\phi = 0.7$. The flame position was estimated to be at the location of the thermocouple with the maximum temperature (i.e. maximum solid phase

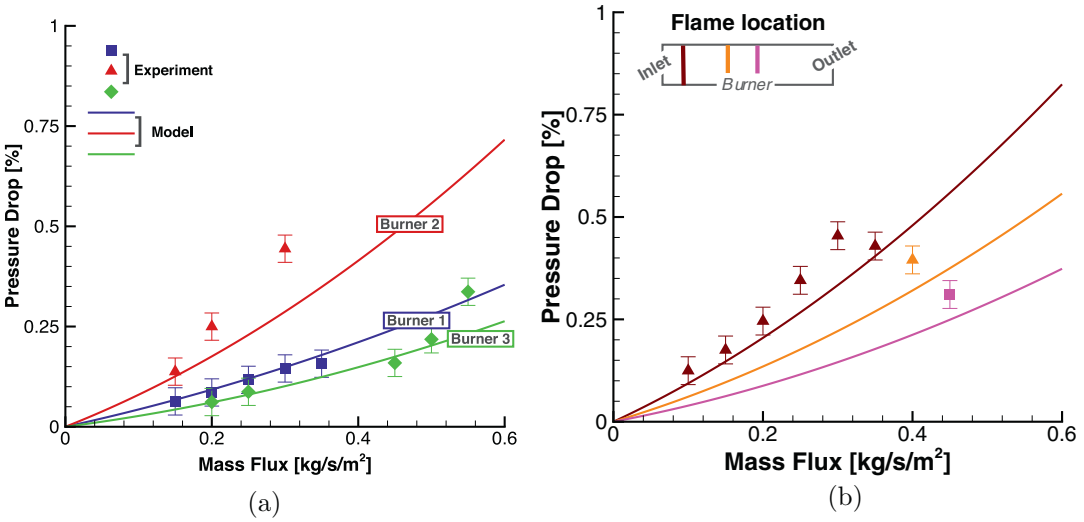

Fig. 5. Comparison of predicted (lines) and experimental (symbols) pressure drop for (a) of all burners at $\phi = 0.6$ and (b) Burner 2 comparing different flame locations at $\phi = 0.7$.

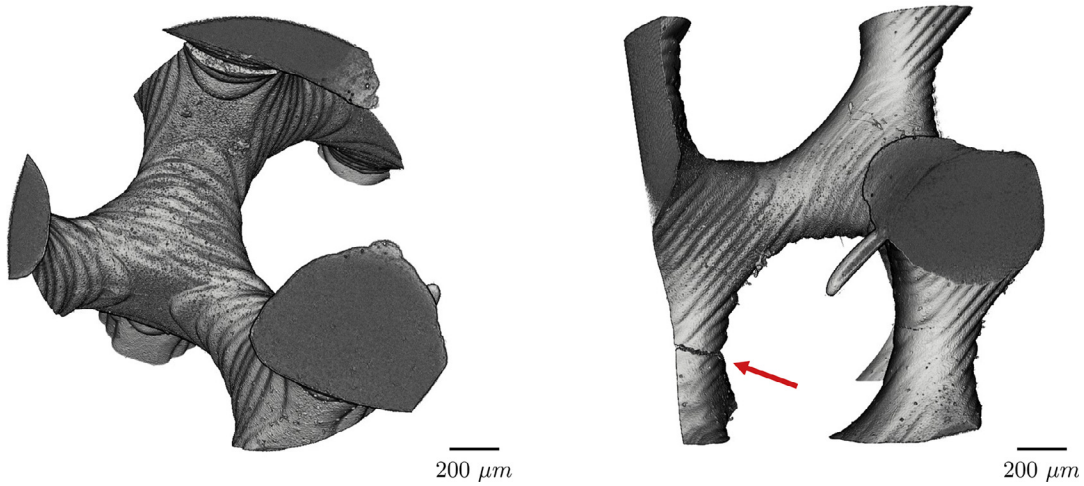

Fig. 6. XCT volume rendering of fragment from the AM ceramic, with arrow showing location of crack formation.

temperature [19]). Previous computational studies have found this location to coincide with that of the peak gas phase temperature in both 1D [22] and in 3D [23]. As the flame stabilized further downstream, the section of the PMB containing burned gas (with lower density and higher viscosity) was smaller, leading to a lower pressure drop. Discrepancies between the predicted and experimental pressure drops may be due to small uncertainties in the exact geometric properties of the burners. To examine the effects of uncertainty in porosity, a sensitivity analysis was performed showing that a variation in porosity of $\pm 2\%$ leads to a variation of approximately $\pm 25\%$ of the estimated pressure drop value. In addition, the precise flame location was unknown given the discrete spacing of the thermocouples, and could have also contributed to the difference in experimental and theoretical values.

5.4. *Porous structure durability*

The layer-by-layer printing procedure of the LCM resulted in unique surface and structural features of the Al_2O_3. Ceramics are notable for their high compressive strength but, are more prone to failure in tension. The tensile or flexural

strength of sintered α-alumina is approximately 0.38 GPa [24]. Flaws, such as cracks or micropores, in a brittle material limit its strength and durability. Fig. 6 shows an XCT scan of a fragment spalled from the burner during operation. The furrows created by the printed layers form regions of high stress concentration, and the maximum tensile stress along these furrows makes the structure prone to cracks in the perpendicular direction, as seen in Fig. 6. Over the course of a few hours of testing, the burners showed signs of cracking due to thermal shock as the flame entered the PMB. A simple materials analysis was performed to provide reasoning for the cracking in the burners. From mechanics, a change in temperature leads to thermal expansion in a material. By modeling the strut as a beam with built-in boundary conditions undergoing axial compression due to thermal expansion, and assuming a constant expansion coefficient, the resulting axial stress can be calculated using $\sigma = \alpha E \Delta T$, where α is the linear thermal expansion coefficient and E is the Young's modulus of the material. For one strut being heated by a flame ($\Delta T = 860$ K), the resulting stress is estimated as 2.4 GPa [24]. Assuming that an identical tensile stress is imposed in another member, this value exceeds the flexural strength of α-alumina, and as a result, the structure would be expected to fail. In future work, strategies will be considered to improve durability, including geometric modifications to redistribute thermo-mechanical stresses, slowly preheating the burner to reduce thermal shocks, and using smaller Al_2O_3 particles to improve sintering.

6. Conclusions

In this study, the feasibility of additive manufacturing of complex ceramic structures with functionally graded geometries was explored and the effects of different burner topologies on PMB performance were experimentally investigated. To experimentally test simulation results and compare graded versus conventional step burners, three different PMBs were synthesized using triply periodic minimal surfaces, fabricated using additive manufacturing, characterized with XCT, and tested over a range of operating conditions. It was shown that the burner graded in pore-diameter enabled flame stabilization at multiple locations without flashback, leading to a significant extension of the stability map in comparison to the equivalent step case. The burner graded in porosity did not stabilize many conditions due to its large inlet pore-diameters, as predicted by computational analysis. Experimental pressure drop for the burners was generally less than 0.5% for most conditions and agreed reasonably well with predicted values, demonstrating the advantages of using XCT analysis to predict experimental performance.

The results in this study confirm concepts in PMB design and demonstrate potential advantages associated with using graded PMBs. Additive manufacturing, in conjunction with well-described geometric surface equations, was successfully employed to tailor burner topology. However, tests showed that the highly regular structure of the burners led to a buildup of stress, which made them prone to cracks and thus limited their structural durability. Further XCT analysis motivates the optimization of the burner geometry and material in future studies.

Declaration of Competing Interest

The authors declare that they have no known competing financial interests or personal relationships that could have appeared to influence the work reported in this paper.

Acknowledgments

This work is supported by a Leading Edge Aeronautics Research for NASA grant (No. NNX15AE42A), the National Science Foundation (NSF) (No. CBET-1800906 and Graduate Research Fellowship with No. 1656518). Part of this work was performed at the Stanford Nano Shared Facilities (NSF No. ECCS-1542152). We would also like to acknowledge Lithoz GmbH for manufacturing the structures used in this study.

References

[1] Y. Kotani, T. Takeno, *Proc. Combust. Inst.* 19 (1982) 1503–1509.
[2] G. Brenner, K. Pickenäcker, O. Pickenäcker, D. Trimis, K. Wawrzinek, T. Weber, *Combust. Flame* 123 (2000) 201–213.
[3] A.J. Barra, J.L. Ellzey, *Combust. Flame* 137 (2004) 230–241.
[4] S. Sobhani, J. Legg, D.F. Bartz, J.J. Kojima, C.T. Chang, J.D. Sullivan, J.P. Moder, M. Ihme, *Combust. Flame* 212 (2020) 123–134.
[5] S. Wood, A.T. Harris, *Prog. Energ. Combust. Sci.* 34 (2008) 667–684.
[6] M.A. Mujeebu, M. Abdullah, M.A. Bakar, A. Mohamad, R. Muhad, M. Abdullah, *J. Environ. Manag.* 90 (2009) 2287–2312.
[7] D. Trimis, F. Durst, *Combust. Sci. Technol.* 121 (1996) 153–168.
[8] S. Sobhani, D. Mohaddes, E. Boigne, P. Muhunthan, M. Ihme, *Proc. Combust. Inst.* 37 (2019) 5697–5704.
[9] P. Colombo, *Philos. Trans. A Math. Phys. Eng. Sci.* 364 (2006) 109–124.
[10] J. Binner, Ceramics Foams, John Wiley Sons, Ltd, pp. 31–56.
[11] D.G. Goodwin, H.K. Moat, R.L. Speth, Cantera: An object-oriented software toolkit for chemical kinetics, thermodynamics, and transport processes, http://www.cantera.org, version 2.3.0 (2017). doi:10.5281/zenodo.170284.

[12] C.T. Bowman, R.K. Hanson, D.F. Davidson, W.C. Gardiner, Jr., V. Lissianski, G.P. Smith, D.M. Golden, M. Frenklach, M. Goldenberg, GRI-Mech 2.11, 1995, Available from http://www.me.berkeley.edu/gri-mech/.
[13] I. Maskery, L. Sturm, A.O. Aremu, A. Panesar, C.B. Williams, C.J. Tuck, R.D. Wildman, I.A. Ashcroft, R.J.M. Hague, *Polymer* 152 (2018) 62–71.
[14] D.J. Yoo, *Int. J. Precis. Eng. Man.* 12 (2011) 61–71.
[15] M. Schwentenwein, J. Homa, *Int. J. Appl. Ceram. Tec.* 12 (2015) 1–7.
[16] S. Sobhani, S. Allan, P. Muhunthan, E. Boigné, M. Ihme, *Adv. Eng. Mater.* 22 (2020) 2000158, doi:10.1002/adem.202000158.
[17] D. Legland, I. Arganda-Carreras, P. Andrey, *Bioinformatics* 32 (2016) 3532–3534.
[18] E. Maire, P. Colombo, J. Adrien, L. Babout, L. Biasetto, *J. Eur. Ceram. Soc.* 27 (2007) 1973–1981.
[19] C. Zheng, L. Cheng, A. Saveliev, Z. Luo, K. Cen, *Proc. Combust. Inst.* 33 (2011) 3301–3308.
[20] S. Sobhani, B. Haley, D. Bartz, J. Dunnmon, J. Sullivan, M. Ihme, Proceedings of the ASME Turbo Expo 2017: Turbomachinery Technical Conference and Exposition, Volume 5C: Heat Transfer, Turbo Expo: Power Land, Sea, and Air, pages V05CT17A001, doi:10.1115/GT2017-63204.
[21] S. Ergun, A.A. Orning, *Ind. Eng. Chem.* 41 (1949) 1179–1184.
[22] A.J. Barra, G. Diepvens, J.L. Ellzey, M.R. Henneke, *Combust. Flame* 134 (2003) 369–379.
[23] C. Bedoya, I. Dinkov, P. Habisreuther, N. Zarzalis, H. Bockhorn, P. Parthasarathy, *Combust. Flame* 162 (2015) 3740–3754.
[24] M. Munro, *J. Am. Ceram. Soc.* 80 (1997) 1919–1928.